

Terahertz quantum cascade lasers — fabrication and characterisation



Politechnika
Wrocławska

Adam Klimont

Faculty of Fundamental Problems of Technology
Wroclaw University of Technology

A thesis submitted for the degree of

Engineer

02-01-2012

Acknowledgements

I would like to acknowledge the European Union, Wroclaw University of Technology and Semiconductor Physics group at Cavendish for funding me through the six months spent in Cambridge. I am very thankful to Prof. Jan Misiewicz for guidance and help with arranging my placement and to Prof. Dave Ritchie for accepting me as a visiting student in his group.

I would also like to thank Dr. Harvey Beere for the willingness to share his knowledge and give advice whenever I needed it, as well as for growing the wafers that I processed. Anthony, Shruti, Yash — I could not imagine more friendly and helpful lab mates, you made my time here most enjoyable.

Contents

Contents	ii
List of Figures	iv
Nomenclature	vi
1 Introduction	1
1.1 THz radiation	1
1.2 Quantum Cascade Laser	2
1.3 Carrier transport	3
1.3.1 Tunnelling	3
1.3.2 Other transport phenomena	4
1.3.3 Current and voltage	5
1.4 Waveguide	6
1.4.1 Surface plasmons	6
1.4.2 Single plasmon	6
1.4.3 Double metal	8
2 Design	9
2.1 Material system	9
2.2 Bound-to-continuum model	9
2.3 V-672	10
2.4 Resonant-phonon design	11
3 Fabrication	14
3.1 Growth	14
3.2 Processing	14
3.2.1 Single plasmon	15
3.2.2 Double metal	17
3.3 Mounting	17
4 Characterisation	19
4.1 Electro-optical characterisation	19
4.2 Spectral characterisation	20

4.3	Absolute power measurement	24
5	Thermocompression bonding	26
5.1	Jig design	26
5.2	Testing the bond	27
6	Conclusions and future work	29
	Bibliography	30

List of Figures

1.1	Schematic diagram of the conduction band in a QCL	3
1.2	Voltage (red) and differential resistance (blue) plotted against current. The diagrams on the top and to the right show alignment of adjacent sequences related to consecutive regions a, b, c and d. Diagram reproduced from [6].	5
1.3	Surface plasmon intensity on the metal-semiconductor boundary[6]	7
1.4	The mode with the highest figure of merit in a typical single plasmon QCL[6]	7
1.5	The mode with the highest figure of merit in a typical metal-metal QCL[6]	8
2.1	Diagram of chirped superlattice QCL design[18]	10
2.2	Calculated band structure of 2.6THz design used in the fabricated two-colour device. The applied electric field is 1.9kV/cm	11
2.3	Comparison between a) the band structure presented by Kumar <i>et al.</i> [11] and b) the band structure calculated with modified version of Freeman's solver. The layer thicknesses starting from the injector barrier are 4.2 /8.5/ 2.3 /9.6/ 3.4 /7.3/ 4.0 / <u>15.3</u> . Al _{0.15} Ga _{0.85} As barriers are shown in bold and the well doped at $2.05 \times 10^{16} \text{cm}^{-3}$ is underlined.	13
3.1	Diagram of a typical MBE grown QCL structure (not to scale). To the right, an active region is shown schematically.	15
3.2	The main steps in the processing of single plasmon QCLs[6]	16
3.3	Image of a single plasmon QCL after cleanroom processing. Image courtesy of C. H. Worrall.	17
3.4	Processing steps of a metal-metal device shown schematically. Two chips are bonded, mechanically polished and etched in citric acid until the etch-stop layer. Then H ₂ SO ₄ : H ₂ O ₂ : H ₂ O solution is used to remove the etch-stop layer and a portion of the doped GaAs.	18
3.5	The device characterised in this thesis, mounted on a copper block and ready to be mounted on a cryostat.	18

4.1	The elements of the setup for light-current-voltage data collection from an internal thermopile[6]	20
4.2	Light-current-voltage data collected for V-672 single plasmon device at 1% duty cycle.	21
4.3	The elements of the setup for spectral data collection using a FTIR spectrometer and a bolometer[6]	22
4.4	Spectral data collected for V-672 single plasmon device at 1% duty cycle.	23
4.5	The elements of the setup for absolute power data collection using a power meter	24
4.6	a) absolute power collected from V-427 device; b) absolute power plotted against applied duty cycle	25
5.1	Left: The jig parts (top view). Part B is used to align the samples and it is only $900\mu\text{m}$ thick. Parts C and D are identical in shape and size. The dark spot in the centre of part C is the recess in which a steel bearing is placed. M6 screws are placed in circular holes near the sides of the parts. Right: the jig as seen from the side. Black arrows indicate the force exerted on the jig parts. . . .	27

Nomenclature

AR Active Region

BtC Bound-to-continuum

CSL Chirped superlattice

CW Continuous Wave

DC Duty Cycle

DM Double Metal (metal-metal)

FTIR Fourier Transform Infra-Red Spectroscopy

IR Infrared

MBE Molecular Beam Epitaxy

QCL Quantum Cascade Laser

RP Resonant-phonon

SP Single Plasmon

Chapter 1

Introduction

1.1 THz radiation

The THz term has been used to describe various spectral ranges but usually its wavelength fits within $100\mu\text{m} - 1\text{mm}$. Historically, there had been a lack of good sources of such radiation, hence the term *terahertz gap*. From the long wavelength side, electronic devices such as Gunn diode were not able to emit radiation with a frequency higher than 0.1THz. From the short wavelength (optical) side, semiconductor band gap is a limiting factor for the formation of light below 15THz. Optically pumped molecular gas lasers were the only fundamental terahertz oscillators available, however their operating frequency was fixed by the properties of the gas used. Various nonlinear media can be used to convert the visible radiation into THz, but they are disadvantageous either in terms of high production costs or a low output power[16]. In the 1980's long wavelength ($\lambda \sim 46\mu\text{m}$) lasers from lead-salt materials were demonstrated[12], but they suffered from ageing and were sensitive to Auger recombination, in which the energy and the momentum of an electron and a hole are transferred to another carrier instead of being emitted as photons.

Potential applications of the THz radiation should be noted, as they are the main motivation for the research on QCLs. Similarly to the X-rays, it can be used in medical imaging. Its energy is much lower and it cannot penetrate deep into the body because of H_2O absorption, but it is still able to reach a tissue infected by several types of cancer. Contrary to the X-rays, it is believed not to make any changes in the tissue. The THz radiation can also be used in personnel imaging, i.e. the detection of dangerous items and explosives. Many of the substances used in such items have their absorption lines in the THz range, therefore it is not only possible to detect an object, but the information about their composition is given. In addition to this, it has been shown that this radiation can be used in non-invasive inspection of paintings and in the quality control of packaged products.

1.2 Quantum Cascade Laser

The first theoretical description of gain in a superlattice was published by Kazarinov and Suris in 1971[10], following the article by Esaki and Tsu[17] in which the authors predicted formation of band structure minizones in a semiconductor multiple heterostructure. In their article Kazarinov and Suris presented a possibility of electromagnetic waves generation as a result of intersubband transitions in quantum wells. Because such a device would be unipolar, transition energies would not be limited by the band gap of the used material. This property was thought to allow the designing of structures emitting radiation of much longer wavelengths than those of conventional semiconductor lasers. The original proposal suffered from several practical limitations, e.g. it was based on the idea of undoped wells and barriers, where electrons injected into the superlattice would form space charge domains, causing electrical instability.

Because of technological limits the fabrication of such structures was impossible until the late 1980's, when Molecular Beam Epitaxy (MBE) allowed semiconductor growth control with nanometre precision. In 1986 fabrication of a unipolar laser was suggested again by Capasso *et al.*[4] and in 1988 by Liu[13]. In 1994 Faist *et al.* demonstrated the first Quantum Cascade Laser (QCL)[5], where they introduced the injector/collector region that served as a reservoir of electrons and solved the electrical instability problem.

Band structure designs of QCLs can differ significantly, but some generic features are common for all of them. Schematic diagram of the conduction band in a QCL is shown in figure 1.1. The structure consists of two semiconductor materials that create wells and barriers. The same sequence is repeated 50-200 times, thus one electron can take part in multiple transitions — hence the name *cascade*. Two regions are marked in the diagram: *injector region* – a set of electronic states which collect carriers from the lower lasing level $|1\rangle$ and inject them into the upper lasing level $|2\rangle$. The injector and active regions usually consist of several wells and barriers. The barrier i is called the *injection barrier* and plays a crucial role in electron transport into the upper lasing level. Population inversion is achieved by means of fast depopulation of the lower state and relatively long lifetime of the upper state. Both conditions are achieved with quantum design; the depopulation usually involves scattering mechanisms, e.g. LO phonon scattering. Transport mechanisms are described in more detail in the next section.

The first QCL emitted at $4.6\mu\text{m}$ and operated up to 90K. Since its demonstration, the performance and spectral range of these devices have increased significantly. In the first years of QCL development, more effort was put into the research of mid-IR emission (λ from $3\mu\text{m}$ to $40 - 50\mu\text{m}$) — at present such lasers are commercially produced and their power reaches several watts in room temperature. However, this thesis will focus on QCLs emitting THz radiation, whose maximum reported power is of the order of several hundreds of milliwatts and the highest operating temperature is 196K[18]. One of the reasons behind the worse

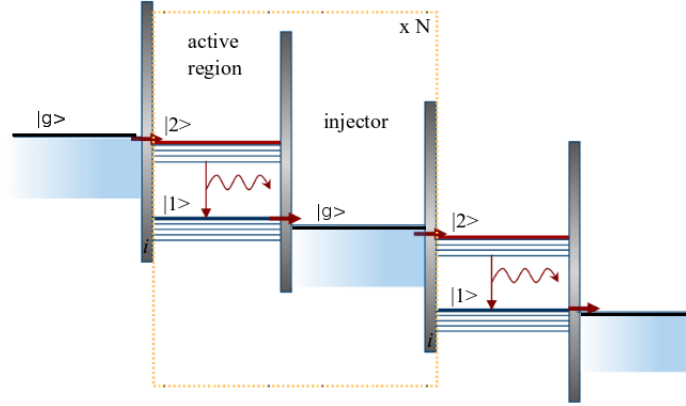


Figure 1.1: Schematic diagram of the conduction band in a QCL

performance of THz QCLs is much lower distance between the lasing states $|2\rangle$ and $|1\rangle$ which makes selective injection to the upper state more difficult.

1.3 Carrier transport

1.3.1 Tunnelling

In all the designs of quantum cascade structures resonant tunnelling plays an important role in electron transport along the superlattice. The diagram in figure 1.1 depicts a superlattice in an external electric field. The slope of the diagram and the position of electronic states depends on the value of the field. For a certain value, the ground state $|g\rangle$ becomes degenerate with the upper lasing state $|2\rangle$ and a resonance is observed in tunnelling from one state to another. It is a necessary condition for the carrier injection into the active region to be efficient. In the tight binding model, the current density can be written as^[10]:

$$J = qN_s \frac{2|\Omega|^2\tau_\perp}{1 + \Delta^2\tau_\perp^2 + 4|\Omega|^2\tau_2\tau_\perp} \quad (1.1)$$

$$\hbar\Delta = E_g - E_3 = qd(F - F_r) \quad (1.2)$$

where q – elementary charge; N_s – sheet density of electrons; d – distance between the centroids of wavefunctions $|g\rangle$ and $|g\rangle$; F – average electric field inside the structure; F_r – the value of electric field for which states $|g\rangle$ and $|2\rangle$ are in resonance; $\hbar\Delta$ – energy difference between $|g\rangle$ and $|2\rangle$; $\Omega = qxF$ – the energy splitting between states $|g\rangle$ and $|2\rangle$ at resonance; τ_2 – state $|2\rangle$ lifetime, and τ_\perp is the relaxation time in the plane parallel to the layers of the superlattice.

When the two states are brought to resonance, i.e. when $\Delta = 0$, the formula for the maximum current density takes the following form:

$$J_{max} = eN_s \frac{2|\Omega|^2\tau_{\perp}}{1 + 4|\Omega|^2\tau_2\tau_{\perp}} \quad (1.3)$$

The value of $4|\Omega|^2\tau_2\tau_{\perp}$ is crucial to transport — depending on its magnitude, a weak or strong injector-excited-state coupling is observed. The former occurs when $4|\Omega|^2\tau_2\tau_{\perp} \ll 1$ and leads to incoherent tunnelling, dominated by scattering.

Strong coupling occurs when $4|\Omega|^2\tau_2\tau_{\perp} \gg 1$. If this is the case, in Eq. 1.3 the current is calculated as:

$$J = \frac{eN_s}{(2\tau_2)^2} \quad (1.4)$$

Upon such conditions carrier injection into the upper lasing state is not limited by the tunnelling rate through the barrier. It should be noted that such conditions do not lead to the maximum possible current density J_{max} , but ensure that the current in the structure is controlled only by one parameter: the lifetime of the excited state $|2\rangle$. For current densities much above the lasing threshold, $4|\Omega|^2\tau_2\tau_{\perp} \gg 1$ might be no longer satisfied as τ_2 decreases because of stimulated emission. Theoretical description of current-voltage characteristics above threshold can be found in source [15].

$|\Omega|$ value much greater than $\frac{1}{\tau_{\perp}}$ may be detrimental, because the oscillator strength of the transition to the lower lasing level $|1\rangle$ would be equally distributed for states $|g\rangle$ and $|2\rangle$ which would lead to the decrease of the gain in $|2\rangle \rightarrow |1\rangle$ radiative transition.

To conclude the above discussion, there are two crucial values controlling transport of the carriers through the injection barrier: $2\hbar|\Omega|$ and τ_2 . There are two ways to increase Ω : either reduce the width of the barrier or design the wave function of $|g\rangle$ state so that the overlap with state $|2\rangle$ is optimised. The shape of the wave function is fully dependent on the design of the whole injection region, i.e. on the widths of the wells and barriers in it.

1.3.2 Other transport phenomena

The tunnelling leads to the phenomenon of negative differential resistance (NDR), i.e. an abrupt increase in voltage while current decreases. NDR was first investigated by Esaki and Tsu[17].

In weakly coupled superlattices high field domains are formed causing different regions of the superlattice to have different electric fields. These domains appear when field coincides with alignment of the lasing states. Another important parameter for a QCL is the level of doping. It must be chosen so that enough carriers are provided to avoid depletion and space-charge formation when operating. At the same time, free carrier absorption should be kept to minimum, which imposes an upper limit for the doping. The exact level of doping is usually determined experimentally[6].

1.3.3 Current and voltage

The current-voltage characteristic of a typical device is shown in figure 1.2. J_{th} is the threshold current and J_{NDR} is the current at which negative differential resistance is observed. Region (a) in the diagram corresponds to zero voltage and no current flowing. In region (b) most of the current flows from one injector to another, the differential resistance is increasing as the width of the channel connecting injectors decreases. Region (c) corresponds to the alignment of the injector ground level with the upper lasing state. The gain is achieved and when it overcomes the loss, J_{th} is reached. In region (d) the structure goes beyond alignment and the resonant channel of electron flow is shut, hence the abrupt increase in voltage. The corresponding decrease in current is mainly due to the loss of photo-induced current. This current can also be seen at J_{th} as a drop in the differential resistance. The magnitude of this drop is related to the ratio of upper lasing state to lower lasing state lifetime[15] and it indicates laser performance.

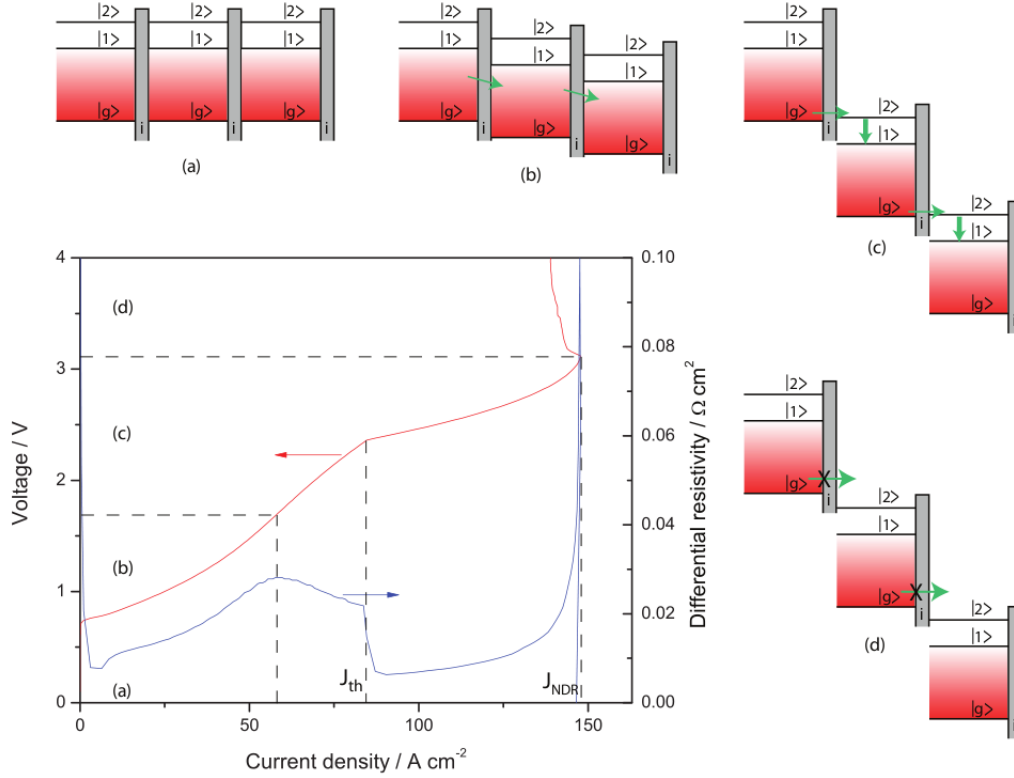


Figure 1.2: Voltage (red) and differential resistance (blue) plotted against current. The diagrams on the top and to the right show alignment of adjacent sequences related to consecutive regions a, b, c and d. Diagram reproduced from [6].

1.4 Waveguide

Waveguide design is crucial to effective emission of radiation from a quantum cascade laser. It is usually characterised by a figure of merit:

$$\beta = \frac{\Gamma}{\alpha} = \frac{\Gamma}{\alpha_w + \alpha_m} \quad (1.5)$$

β is given in units of length, usually centimetres. α_m represents mirror losses; α_w (waveguide losses) comprises of two phenomena: Drude losses in a doped semiconductor material and intersubband absorption of radiation. Γ is a measure of overlap between the active region and the optical mode:

$$\Gamma = \frac{\int_{AR} E_z d\tau}{\int_T E_z d\tau} \quad (1.6)$$

E_z is the component of the electric field perpendicular to the plane of GaAs/AlGaAs layers. The integral in the numerator is taken over the whole active region stack, whilst the one in the denominator — over the volume of the mode. Γ can be calculated[8] and for single plasmon devices it is around 30%.

Traditional laser diodes and mid-IR QCLs use refractive index mismatch in semiconductor claddings as a means to provide a waveguide. Thicknesses of claddings needed for THz lasers are above $100\mu\text{m}$, which is usually too thick especially if it needs to be grown by MBE, therefore other solutions are used, i.e. surface plasmons.

1.4.1 Surface plasmons

A surface plasmon is an oscillation of electric field occurring at the boundary of two materials dielectric constants of which have opposite signs, e.g. metal and semiconductor. Electric field vector is then perpendicular to the junction and to the direction of propagation of these oscillations. The maximum intensity of a plasmon occurs at the interface and decays exponentially in the material. In figure 1.3 the decay is shown in a diagram.

1.4.2 Single plasmon

Single plasmon, or more accurately plasmon-quasi-plasmon devices are fabricated by depositing a metal layer on the top of the active region stack. At the bottom, the AR is bounded by highly doped GaAs layer which has a slightly negative dielectric constant. A plasmon propagates in it, but it is more weakly bound than a plasmon on a metal-semiconductor junction. In figure 1.4 it is shown that the majority of the optical mode is outside the active region and highly doped substrate, therefore the overlap with the AR is low – usually around 30% – but the loss is relatively low as well, around 5cm^{-1} .

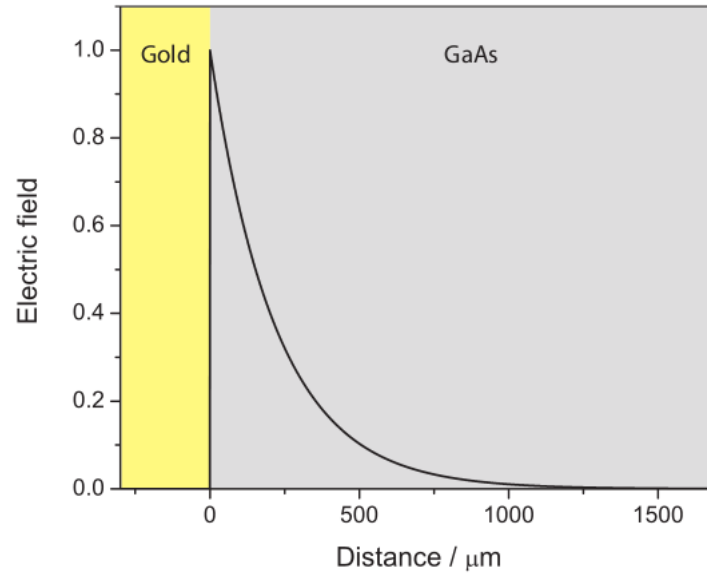


Figure 1.3: Surface plasmon intensity on the metal-semiconductor boundary[6]

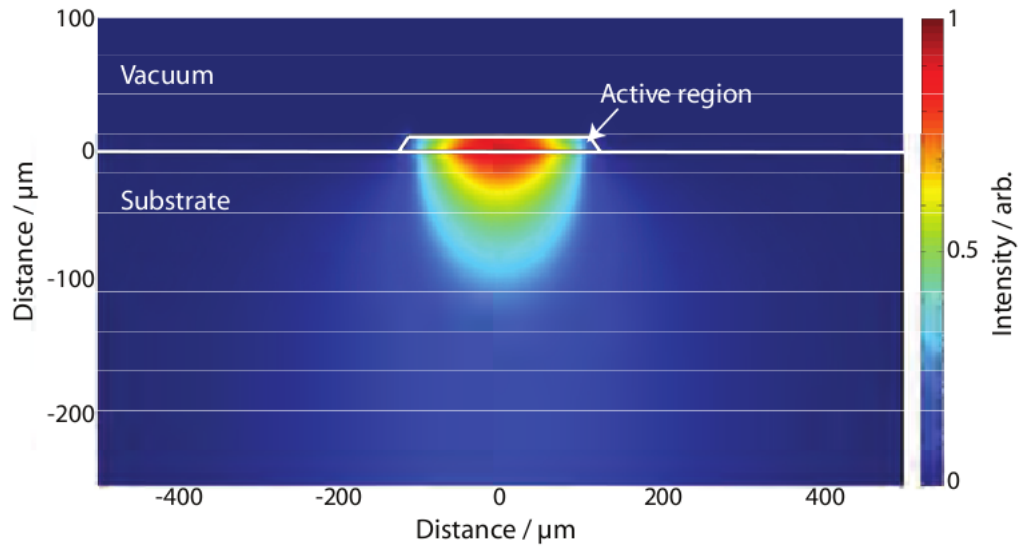


Figure 1.4: The mode with the highest figure of merit in a typical single plasmon QCL[6]

1.4.3 Double metal

Metal-metal waveguides confine the active region stack between two metal layers. The overlap in these waveguides is close to 100% (see figure 1.5), but the losses are higher, 20cm^{-1} . Double metal outperform single plasmon devices especially for long wavelengths ($\lambda > 150\mu\text{m}$) where the overlap in SP waveguides drops significantly, whilst in DM it remains constant. A metal layer below the AR also provides better thermal conductivity, thus improving temperature performance of a laser. A major disadvantage of DM waveguides is low output power caused by the impedance mismatch between the optical mode and the free space resulting from the facet size being smaller than the wavelength.

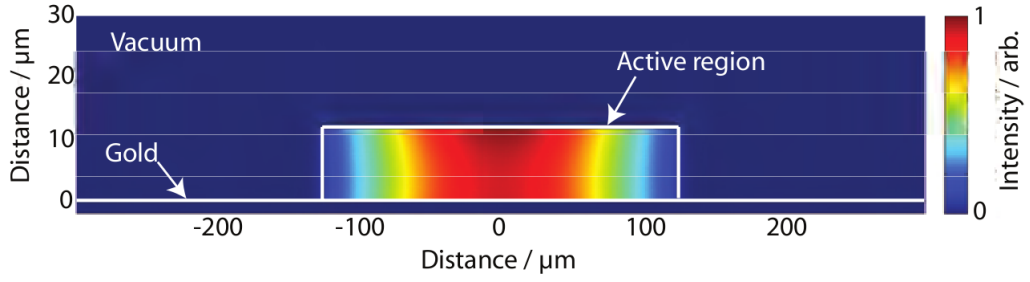


Figure 1.5: The mode with the highest figure of merit in a typical metal-metal QCL[6]

Chapter 2

Design

The device in this thesis is designed to emit two different frequencies for different current densities applied. This was achieved by incorporating two active regions into one wafer by means of MBE. The first stack is designed for 2.9THz emission and the second for 2.6THz. Both active regions use a *bound-to-continuum* (BtC) design and are fabricated in GaAs/AlGaAs material system.

2.1 Material system

The material system used for most THz QCLs is GaAs (wells)/AlGaAs (barriers) grown on GaAs substrate. Although $\text{In}_{0.52}\text{Al}_{0.48}\text{As}/\text{In}_{0.53}\text{Ga}_{0.47}\text{As}$ structure grown on an InP substrate was demonstrated by Ajili *et al.*[1], GaAs/AlGaAs system remains the most used because of its maturity and ability to produce results of high quality, e.g. the highest electron mobility. Beere *et al.*[2] demonstrated how important the quality of growth was to the performance of QCLs. One of the major advantages of GaAs/AlGaAs material system is that GaAs and AlAs have almost the same lattice constants, therefore AlGaAs is lattice matched to GaAs independently of Al concentration. In this thesis Al concentration of 0.15 has been used. It is worth noting that less aluminium allows growing slightly thicker layers and hence more accurate growth.

2.2 Bound-to-continuum model

Before describing the BtC design, it is vital to mention its predecessor, i.e. *chirped superlattice* (CSL) model. A schematic diagram of the latter is shown in figure 2.1. Electronic states in several adjacent wells are strongly coupled to each other and give rise to a *miniband*. Radiative transition takes place between the lowest state of the upper miniband $|2\rangle$ and the highest state of the lower miniband $|1\rangle$ — similarly to interband transitions in standard semiconductor lasers. Population inversion is achieved because scattering processes inside a miniband occur at a

faster rate than inter-miniband scattering. As a result, electrons relax into the lower energetic states, leaving the upper states relatively empty.

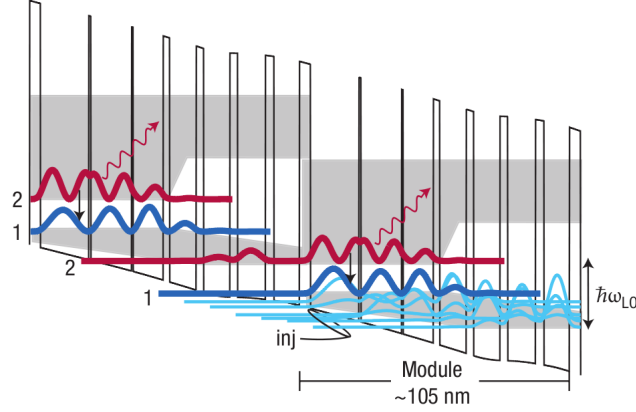


Figure 2.1: Diagram of chirped superlattice QCL design[18]

In the BtC design, the lower lasing state and miniband depopulation model remain the same, but the upper lasing state is made to be a bound *defect* state in the gap between minibands. The resulting optical transition is more diagonal in real space. Overlap between the bound state and the lower miniband decreases and so does the oscillator strength, but the lifetime of the upper lasing state increases as a result of reduction in non-radiative scattering. The injector states are more strongly coupled to the bound state and more weakly coupled to the lower miniband which ensures better injection selectivity. On overall, devices based on BtC design have shown better temperature and power performance than CSL QCLs.

2.3 V-672

The device in this thesis was fabricated from MBE wafer V-672. Two active region stacks were incorporated into the wafer, one designed to emit radiation at 2.6THz, another at 2.9THz. The layer thicknesses of the former starting from the injector barrier are **3.8**/11.6/**3.1**/10.7/**2.4**/10.5/**1.8**/11.0/**1.8**/13.4/**2.0**/13.9/**1.7**/13.6 / **0.6**/9.0/**0.7**/16.6, and those of the latter are **3.5**/12.2/**3.2**/11.9/**2.5**/12.0/**1.8** / 12.7/**1.8**/12.9/**1.6**/13.5/**1.4**/16.7/**0.5**/9.5/**0.5**/14.8. $\text{Al}_{0.15}\text{Ga}_{0.85}\text{As}$ barriers are shown in bold and wells doped at $1.3 \cdot 10^{16}\text{cm}^{-3}$ are underlined.

figure 2.2 depicts band structure of the 2.6THz design. Two repeats of the periodic sequence are shown. At the bottom a miniband can be seen consisting of a number of closely spaced electronic states. The lowest state of the miniband $|g\rangle$ is plotted in blue, the upper lasing state $|2\rangle$ in green, and the lower lasing state $|1\rangle$ in red. $|1\rangle$ is the highest state in the miniband.

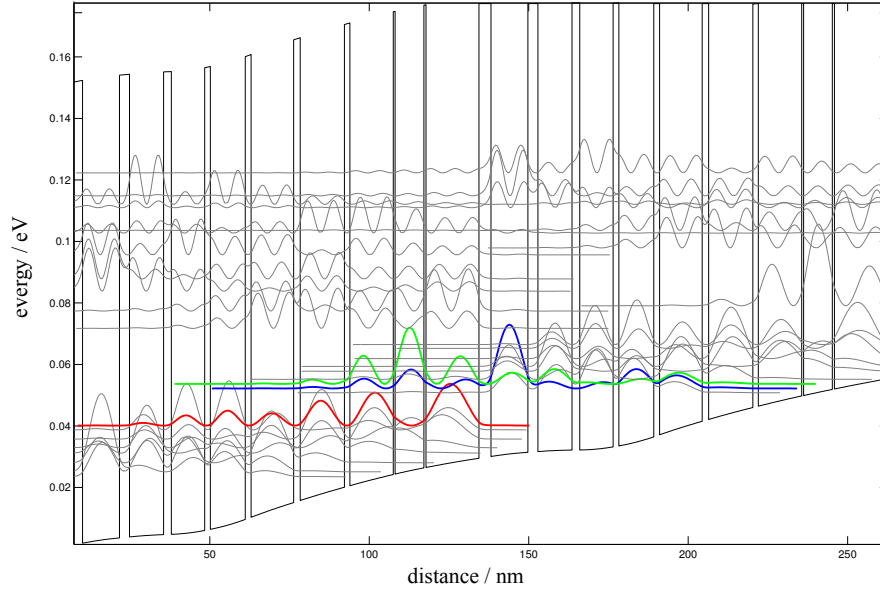


Figure 2.2: Calculated band structure of 2.6THz design used in the fabricated two-colour device. The applied electric field is 1.9kV/cm

The structure is solved for two periods of the active region. The solution yields lasing at 2.91THz. Band structure calculations were performed with a modified version of the program written in Fortran by Dr. Joshua Freeman, based on the finite element method[14]. The program solves the one band Schroedinger model iteratively in conjunction with the Poisson equation to converge at a self-consistent solution. Details of the 1D formulation of the Schroedinger equation in the finite element approach can be found in source[6]. The experimental results obtained from this structure are demonstrated in Chapter 4.

2.4 Resonant-phonon design

Recently, there has been much interest in resonant-phonon THz QCLs[9, 18]. The main difference from the previous designs is the depopulation mechanism: here, the upper lasing state and the lower lasing state are separated by 36meV, i.e. the energy of longitudinal phonons in gallium arsenide. It allows the electrons to depopulate the lower state at a very high rate by means of emitting an LO phonon. This design had already been successfully implemented in mid-IR QCLs. However, in THz laser designs the upper and lower states are very closely spaced, therefore THz resonant-phonon QCLs suffered from the fast depopulation of both states. The solution to this problem was to design the lower state's wave function so that it spread over several adjacent wells, improving the overlap with the

injector states lying below. At the same time, the upper state remains strongly localised and it has very little overlap with the injector states.

A modified RP (*scattering-assisted*) design was presented by Kumar *et al.*[11]. The demonstrated device emitted radiation at 1.8THz and showed surprisingly good temperature performance, therefore the Semiconductor Group at Cambridge would like to move to this kind of QCL design. However, the essential tool needed for the designing is a solver application. The one written by Dr. Joshua Freeman was optimised for solving BtC structures and it seems that it needs to be modified in order to produce reliable results for other designs.

An attempt was made to simulate the aforementioned structure. The first result was not satisfactory and quantitatively different from the diagram in the paper. Then the script was changed to truncate the electronic wave functions at the ends of each period. This is physically less favourable but in some cases it facilitates the convergence of the solution. With such settings, the solver yielded a band structure similar to that of the original article. It may indicate that Kumar and others used a solver that truncates the wave functions even the diagram in their paper (reproduced in figure 2.3a)) suggests this method.

Because BtC designs distinguish only three crucial states: injector, upper and lower, the script had to be adjusted so that it displayed all five states important to the Kumar design and calculated the transition energy between appropriate states. Qualitatively, the comparison is represented in figure 2.3. Slight discrepancies can be seen, but the shape and position of all wave functions are preserved. In terms of quantities, the only value that can be compared is the transition energy. According to the paper, it is equal to 1.8THz. Unfortunately, it is not certain (no Y axis in the diagram) whether it was designed to lase at 1.8THz or it happened to emit radiation at this frequency. The calculations with aforementioned solver yielded 1.93THz transition. It is difficult to compare the energy spacing between levels 3 and 2 because in the Kumar's paper it is only shown as around ω_{LO} . Freemans solver calculated a value of 41.8meV, which is slightly more than the resonant LO phonon energy (36meV).

To conclude this section, the available solver produces results that are similar to those of other groups. However, the discrepancies need to be investigated and their origins found in order to obtain reproducible and reliable simulations.

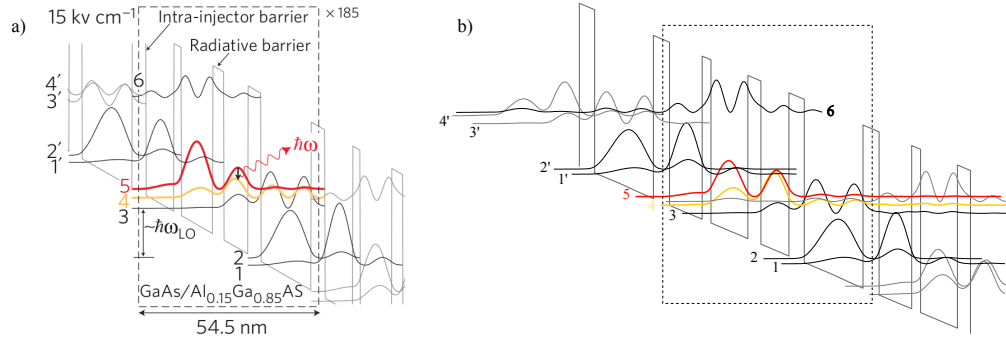


Figure 2.3: Comparison between a) the band structure presented by Kumar *et al.* [11] and b) the band structure calculated with modified version of Freeman's solver. The layer thicknesses starting from the injector barrier are **4.2/8.5/2.3/9.6/3.4/7.3/4.0/15.3**. $\text{Al}_{0.15}\text{Ga}_{0.85}\text{As}$ barriers are shown in bold and the well doped at $2.05 \times 10^{16} \text{ cm}^{-3}$ is underlined.

Chapter 3

Fabrication

3.1 Growth

The devices described in this thesis have been grown in Veeco ModGen II MBE chamber. A GaAs substrate is placed in the middle of the chamber on a heated holder. Inside the chamber, a very high vacuum is maintained. The sample can be rotated to ensure uniform growth. Around the holder are mounted effusion cells, each of which contains an element of a very high purity: gallium, arsenic, aluminium. The cells are heated and the atoms are directed onto the substrate. Shutters are used to control the composition of each of the elements. In such a system, layers can be grown with subnanometer precision.^[2]

A typical cascade structure is shown schematically in figure 3.1. The starting point is a (100) semi-insulating GaAs 500 μm thick wafer. After a thin buffer layer of GaAs, 300nm of $\text{Al}_{0.5}\text{Ga}_{0.5}\text{As}$ is deposited, which serves as an etch-stop in metal-metal device processing. The next layer is 700 μm thick Si-doped GaAs. Its function is twofold: firstly, it is an electrical contact in a mounted device; secondly, in single plasmon devices it plays a role in the formation of a quasi-plasmon. The next layers are the core of a QCL: these are repeated sequences of quantum wells and barriers consisting of GaAs and $\text{Al}_{0.15}\text{Ga}_{0.85}\text{As}$. The fraction of aluminium might change in different designs — here, that of the characterised devices is used. The number of repeats usually varies from 50 to 100 and each repeated sequence consists of 5-10 layers a few nanometres thick. Often 2 or 3 of these are silicon doped. The growth ends with a 80nm highly doped GaAs which ensures top electrical contact.

3.2 Processing

The wafer removed from the MBE chamber may be processed into a working laser by the use of two different methods: into a single plasmon and a double metal device. The device in this thesis was fabricated using the single plasmon

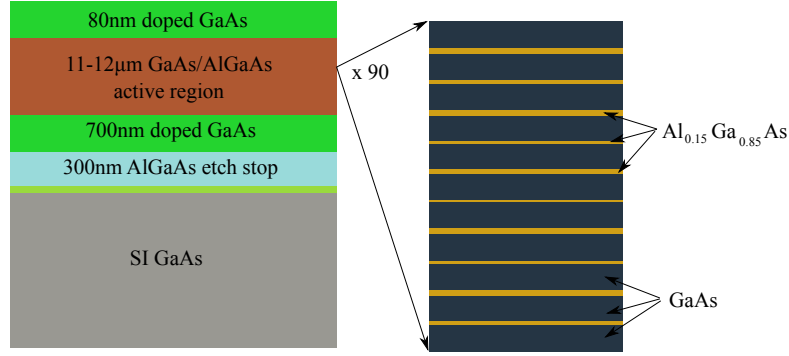


Figure 3.1: Diagram of a typical MBE grown QCL structure (not to scale). To the right, an active region is shown schematically.

waveguide, but it is plausible to briefly describe metal-metal fabrication as well, as it will be referenced in chapter 5.

3.2.1 Single plasmon

Consecutive steps of sample processing are schematically shown in figure 3.2. From the MBE grown substrate 5mm x 6mm chips are cleaved, on each of which eventually three laser ridges are processed.

The chip is placed on a spinner, Shipley S1813 photoresist is put on it and it is spun at 5000 rpm for 30-60s. After spinning it is baked for a minute on a hot plate at 90°C. The resist should be around 1.1μm thick. Next, a mask aligner is used to align a metal mask with the sample and it is then exposed to UV light for a few (6-8) seconds. The last lithography step is developing the pattern on a chip with MF-319 developer for 60-90s. For devices described in this thesis a positive resist is used, i.e. the resist which has been exposed is later developed. The use of *UV lithography* term below will always mean the exact process described above, unless stated otherwise.

The first aligned pattern is the laser ridge. Its dimensions are approximately 3,5mm x 200μm. It is then etched in H₂SO₄ : H₂O₂ : H₂O solution. The composition of the solution is chosen to match the desired etch rate and sidewalls profile. The devices described in this thesis were etched in (1:8:40) proportion, respectively, which yields the etch rate of about 0.9 $\frac{\mu\text{m}}{\text{min}}$ and sidewalls slope of 45°. The etching depth is calculated basing on the basis of the growth sheet of a wafer, so that 300-400nm of bottom GaAs layer is left unetched.

The next step is to place bottom contacts on the sides of the ridge. The lithography is performed with a slight modification (used when developing a pattern is followed by metal evaporation): after exposing to UV light, the chip is dipped in chlorobenzene for 3 to 5 minutes. The substance hardens the surface of the resist and allows easier *lift-off* after metal evaporation. After developing

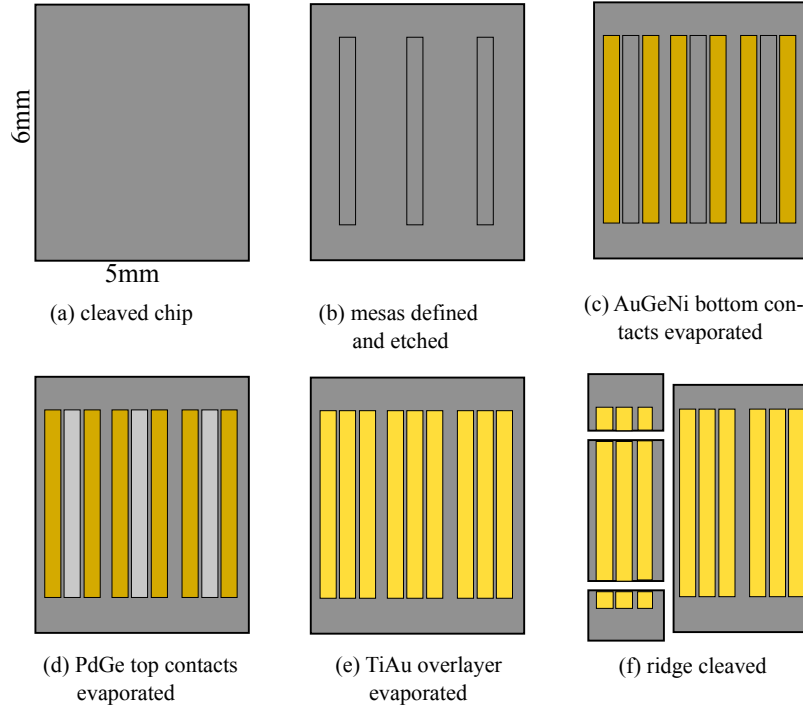


Figure 3.2: The main steps in the processing of single plasmon QCLs[6]

the appropriate pattern, 100nm of AuGeNi (88:12:5 by molecular weight) is evaporated and then lifted off in acetone. Afterwards annealing at 450°C is carried out on the sample in order for the alloy to spike down through several hundreds of nanometres of the underlying GaAs. An ohmic contact is formed instead of a Schottky junction, which provides an effective carrier transport through the structure.

Afterwards, evaporation is carried out to deposit Pd(25nm)/Ge(75nm) top contact. Because this process is especially vulnerable to the external conditions, it takes place in an electron beam evaporator in vacuum lower than $5 \cdot 10^{-8}$ mbar. This metal layer is then annealed in 350°C and the resulting ohmic contact is shallower than the previous one. The Pd/Ge contact is responsible for creating a plasmon on the metal-semiconductor junction.

The last lithography and evaporation steps lead to the deposition of an overlayer of titanium (15nm) and gold (100nm). Its function is twofold: it facilitates wire bonding of the device and improves the quality of the plasmon created by Pd/Ge layer.

After depositing the aforementioned layers, the back-side of the sample is mechanically ground in order to thin the host GaAs substrate. It improves the thermoconductive properties, which are essential for heat sinking when the device is mounted. Then a backside Ti/Au evaporation is carried out in order to facilitate soldering the device with indium and prevent the diffusion of indium

into the substrate. An image of a device processed with aforementioned steps is shown in figure 3.3.

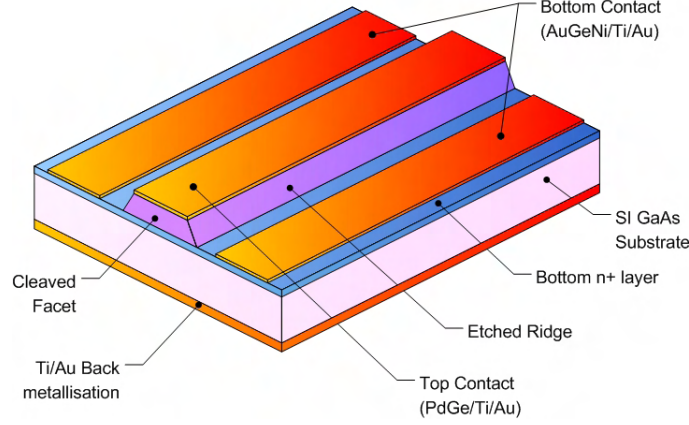


Figure 3.3: Image of a single plasmon QCL after cleanroom processing. Image courtesy of C. H. Worrall.

3.2.2 Double metal

The processing of a metal-metal waveguide is more difficult and time consuming, however the performance of a DM device in terms of operating temperature and threshold current is better. The first step of this process is cleaving a piece of MBE material, evaporating Pd/Ge on it and annealing it at 350°C for 300s in order to obtain a shallow ohmic contact, analogously to the SP process. Then a chip of n^+ (highly doped) GaAs is cleaved to the same size and a thick layer of Ti (20nm)/Au (600nm) is evaporated on both pieces. These two gold layers allow Au-Au thermal compression bond, which will be described in detail in chapter 5.

After bonding, the next step is to remove the substrate from the MBE grown chip. First it is mechanically polished to remove a large amount of the GaAs. Then it is selectively etched in citric acid ($C_6H_8O_7 : H_2O_2$ 5:1). This mixture etches GaAs and $Al_{0.5}Ga_{0.5}As$ with a ratio approximately 120:1, respectively. The etching stops at AlGaAs layer, removing all of the substrate. Then $H_2SO_4 : H_2O_2 : H_2O$ solution is used to remove the etch-stop layer and a significant portion of the adjacent doped layer, as shown in figure 3.4. Once these steps have been completed, the chip is processed similarly to a single plasmon waveguide, but the exact steps are not relevant to this thesis.

3.3 Mounting

Cleaved ridges are ready to be mounted on copper blocks using indium solder. On the sides of the devices three pads coated with gold are glued, to which golden

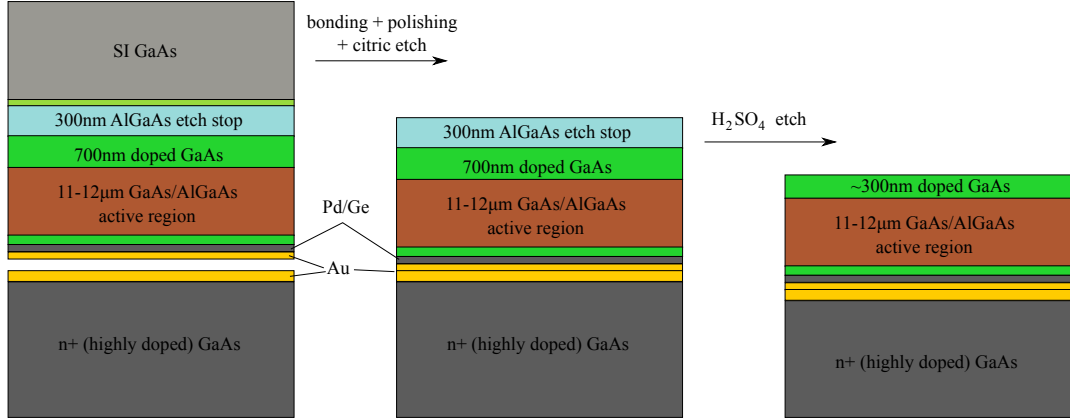


Figure 3.4: Processing steps of a metal-metal device shown schematically. Two chips are bonded, mechanically polished and etched in citric acid until the etch-stop layer. Then $\text{H}_2\text{SO}_4 : \text{H}_2\text{O}_2 : \text{H}_2\text{O}$ solution is used to remove the etch-stop layer and a portion of the doped GaAs.

wires are attached — usually as many as the ridge length allows, because the more wires, the more uniform electric field in the structure and the lower the current passing through each wire. After all the above processing steps, the laser is ready to be put on a cold finger of a cryostat, contacts of which are connected with coated pads on the copper block. In figure 3.5 a picture of a fully processed QCL is shown.

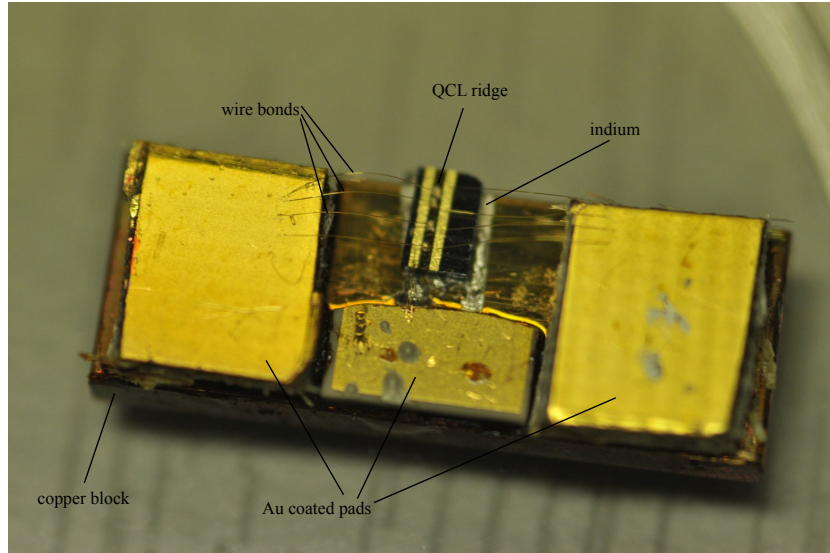


Figure 3.5: The device characterised in this thesis, mounted on a copper block and ready to be mounted on a cryostat.

Chapter 4

Characterisation

The device described in this thesis was characterised in two distinct experiments. The purpose of the first one was to measure the output power and current-voltage characteristics, and the second one was conducted in order to obtain the emitted spectrum as a function of current density. The measurements can be taken in either pulsed or continuous wave (CW) mode. The former has been chosen because it requires less setting up time and provides better signal to noise ratio. Moreover, heating of the device in CW mode often results in poor repetitiveness of the experiment.

4.1 Electro-optical characterisation

The setup for light-current-voltage (LIV) measurement is shown schematically in figure 4.1. The QCL can be contacted in two or three terminal configuration. In the former, the current is passed through both bottom contacts, reducing the contribution of the bottom GaAs layer. Unfortunately, electric field is less uniform in this case as it is difficult to wire bond the device symmetrically. In the following experiment two terminal configuration was used to obtain better QCL performance.

The detector is a thermopile mounted in one of the windows of a cryostat. A pulse generator powers the QCL with a 10kHz square wave and a 1% duty cycle. The resulting pulse is $1\mu s$ long, which is short enough so as not to cause significant heating of the device. The pulse generator is gated by a function generator with a response frequency of the detector, 4Hz. The same frequency is passed as a reference signal to a lock-in amplifier fed by the thermopile output and also triggers an oscilloscope. The current through the device is measured by a current pick-up coil connected to the oscilloscope and the voltage across the QCL is also measured by this oscilloscope. The instruments are controlled and the output collected by a LabView program on a computer.

The measured device was fabricated into a single plasmon waveguide from MBE wafer V-672 described in Section 2.3. The ridge was cleaved to $2.99\text{mm} \times 250\mu\text{m}$,

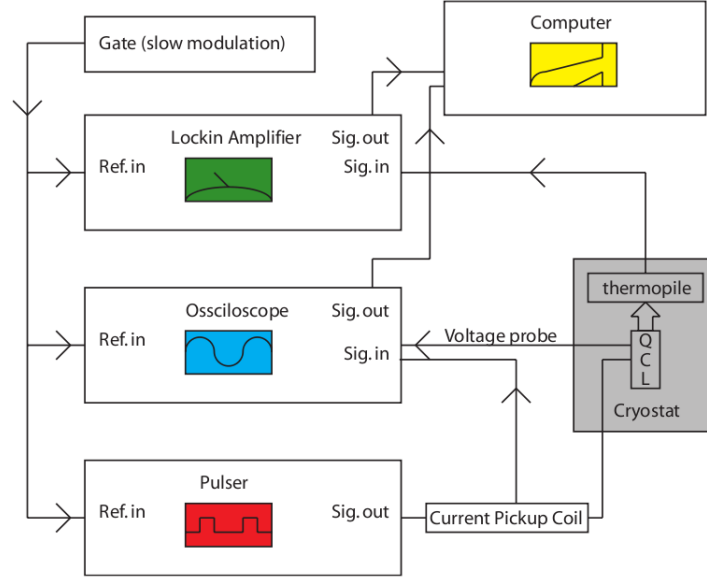


Figure 4.1: The elements of the setup for light-current-voltage data collection from an internal thermopile[6]

packaged, put into a cryostat and cooled with liquid helium. The light-current-voltage plot is shown in figure 4.2. The performance of the laser deteriorates with increasing temperature. The highest temperature at which the QCL emitted radiation was 65K. The threshold current is proportional to the temperature according to the formula:

$$J_{th} = J_0 + \exp(T/T_0) \quad (4.1)$$

The current density of the peak performance at 4K is 170A/cm² for the 2.9THz active region and 205A/cm² for the 2.6THz AR. At 185A/cm², the 2.9THz emission switches off and lasing at 2.6THz is seen, albeit four times weaker than the former. The difference might be caused by various factors, such as fabrication steps or the growth quality. In general, metal-metal devices show better performance in multiple-frequency designs[6], however V-672 has not been fabricated into DM waveguide to check if this was the case.

4.2 Spectral characterisation

To measure the emitted spectrum, a Bruker IFS/66V Fourier transform infra-red (FTIR) spectrometer is used. Its core is a Michelson interferometer connected to a computer. The radiation from the QCL is collected by a set of mirrors and passed on a 50/50 beam splitter. One half is directed onto a fixed mirror and another onto a scanning mirror. The two beams are then rejoined on the

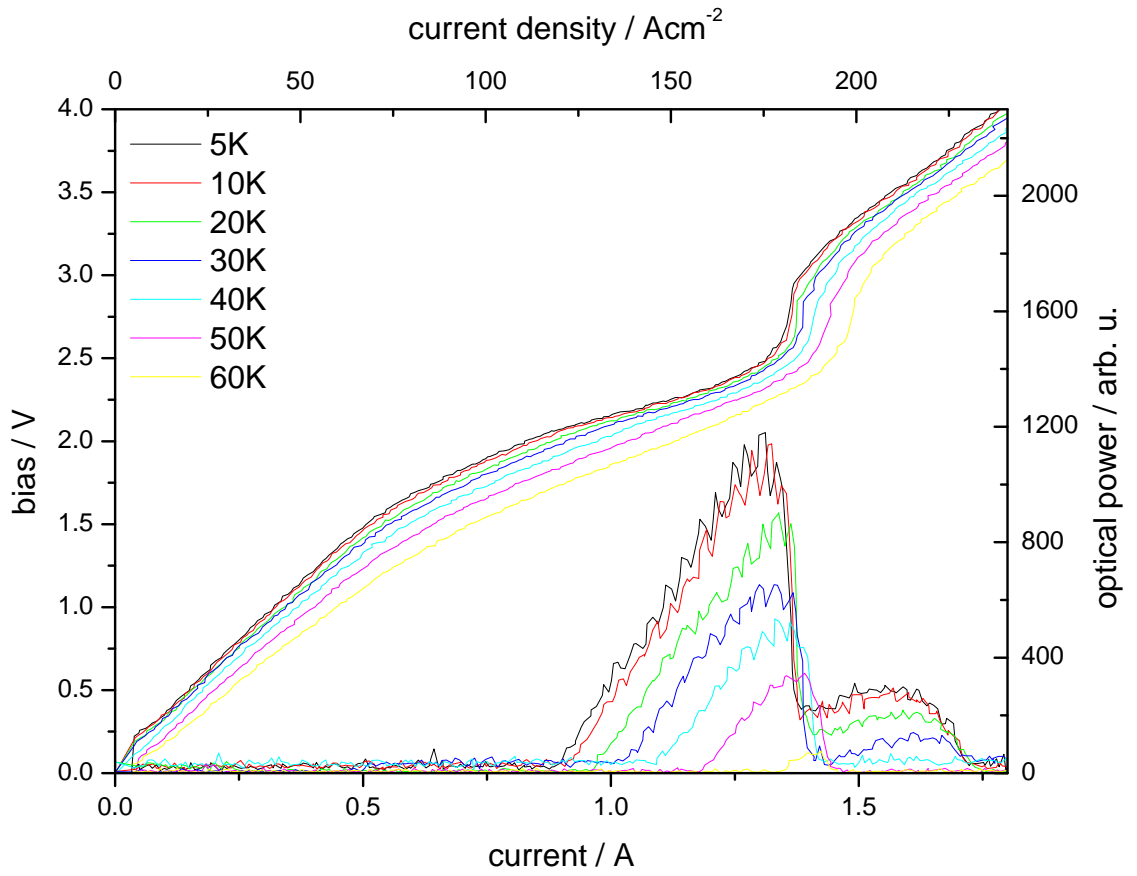


Figure 4.2: Light-current-voltage data collected for V-672 single plasmon device at 1% duty cycle.

beam splitter and collected by a liquid helium cooled bolometer. A sinusoidal modulation of the detected intensity is caused by altering the length of one arm of the interferometer by the scanning mirror. A fast Fourier transform is then performed on the collected signal by the computer and the frequency of the radiation is obtained. The experimental setup for this measurement is shown schematically in figure 4.3.

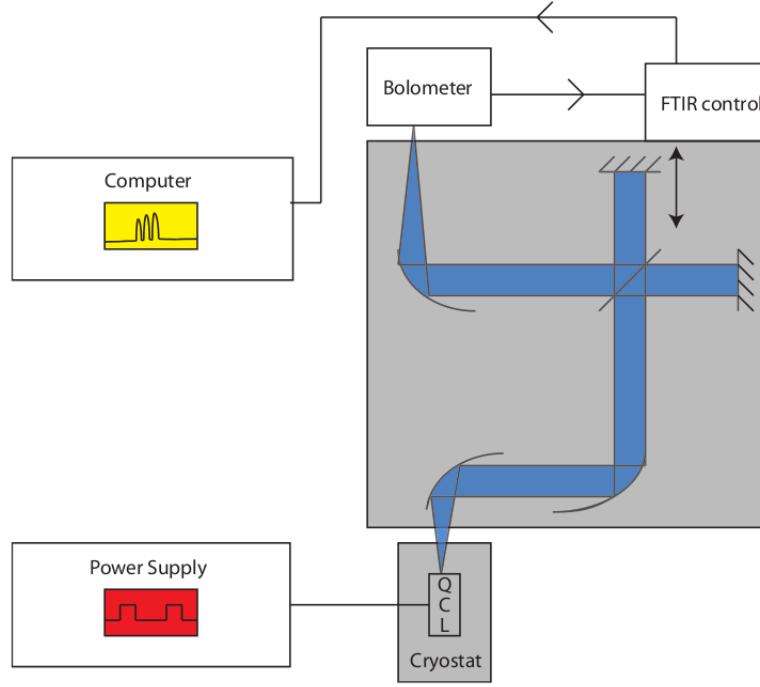


Figure 4.3: The elements of the setup for spectral data collection using a FTIR spectrometer and a bolometer[6]

In figure 4.4 spectral data collected with FTIR spectrometer and a bolometer are shown. The base mode of the 2.9THz design starts lasing at 118 A/cm^{-2} and its frequency is measured as 2.95THz, slightly different from the calculated value. Between 165 A/cm^{-2} and 190 A/cm^{-2} simultaneous emission of two frequencies was observed when the fundamental mode from 2.6THz AR switched on. The frequency of this mode matches the calculated value. The 2.6THz stack continues to lase until 190 A/cm^{-2} . Similarly to LIV measurement, in this experiment much lower intensity of the second active region was observed.

This device could be used as an electronically switchable QCL, but its dual frequency emission capabilities are limited. It has been reported that metal-metal devices are more suitable for dual frequency QCLs, therefore this fabrication method could be used to achieve it. Moreover, the emission at 2.6THz is significantly weaker than that of 2.95THz even in its peak — ideally they should be equal.

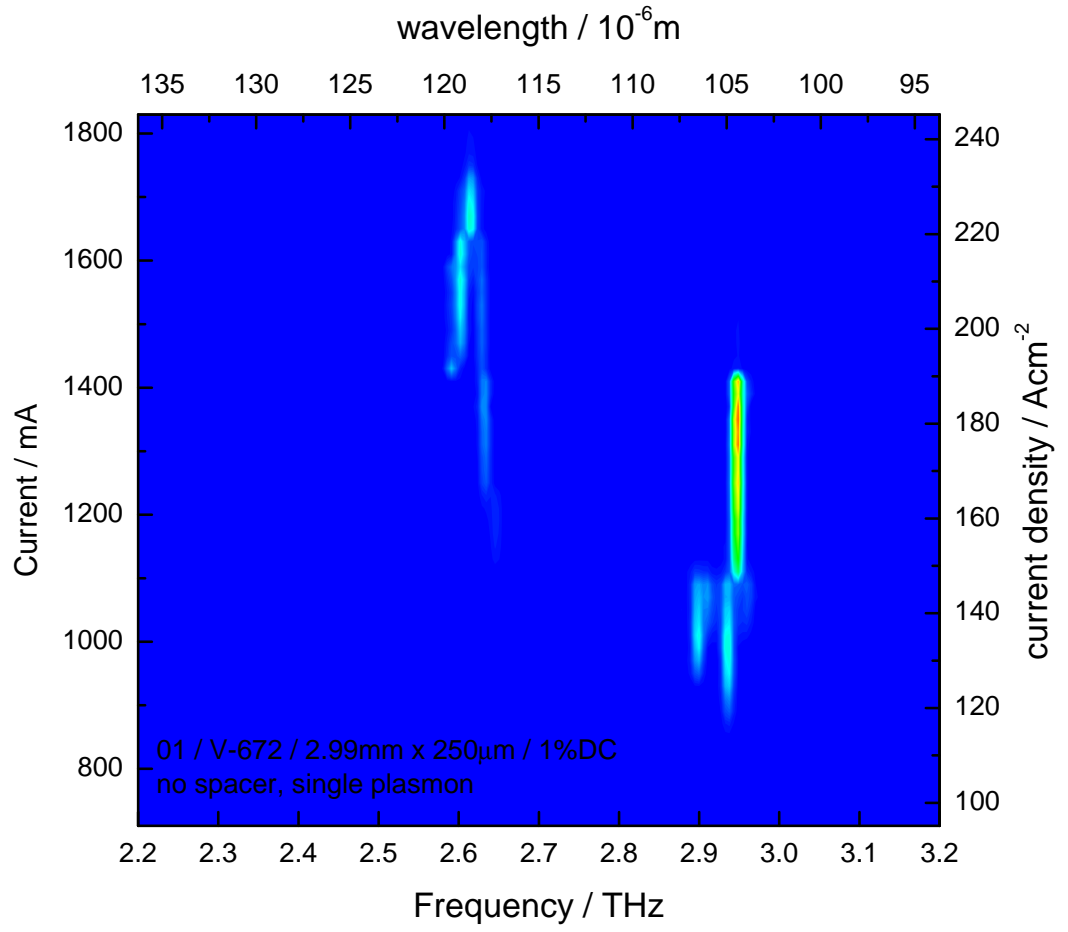


Figure 4.4: Spectral data collected for V-672 single plasmon device at 1% duty cycle.

4.3 Absolute power measurement

The detector is a power meter placed 10cm from the QCL in a cryostat (figure 4.5). A pulse generator powers the QCL with a 10kHz square wave and the duty cycle can be changed in the range 1%-35%. The pulse generator is gated by a function generator with the frequency of 10Hz, which is passed to the computer as a reference signal. The current through the device is measured by a current pick-up coil connected to the oscilloscope and the voltage across the QCL is also measured by this oscilloscope. Similarly to the LIV experiment, the instruments are controlled and the output collected by a LabView program on a computer.

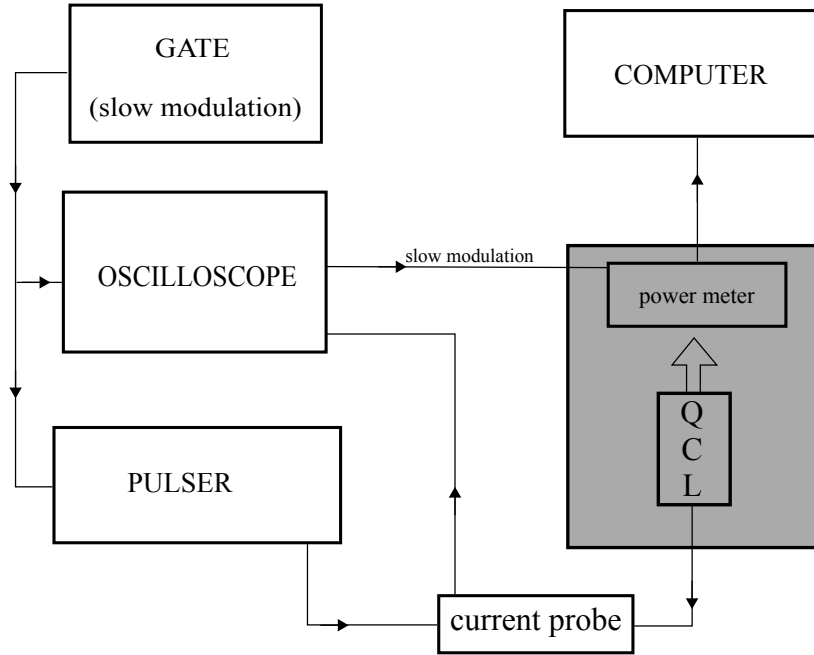


Figure 4.5: The elements of the setup for absolute power data collection using a power meter

The measured laser was fabricated from V-427 wafer which is a BtC structure designed to lase at 2.7THz. Its spectral and LIV performance had been already measured and several devices were reported to work properly, making it a good candidate for further assessment and for a THz source in various experiments in other research groups. Figure 4.6 a) shows the measured data from the device and power as a function of duty cycle is shown on figure 4.6 b).

35% DC was the limit set by the power supply. A proportional increase in absolute emitted power is expected with the rise of duty cycle. Nevertheless, a decrease is observed above 20%. This is anomalous and it had not been observed before. It may come from a ground loop in the setup and subsequent electrical pick-up by the power meter but the reason has not been found yet. The first

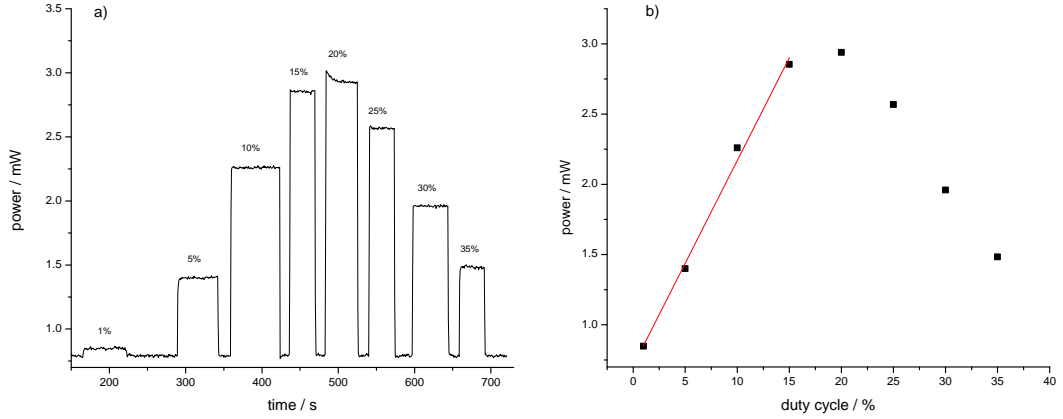


Figure 4.6: a) absolute power collected from V-427 device; b) absolute power plotted against applied duty cycle

four points match the linear fit very well, thus the output power in continuous wave (CW) emission may be predicted from this fit. The calculated intercept is 7.07×10^{-4} and the slope equals 1.46×10^{-4} , thus the extrapolated power at 100% DC (=CW) is 15.4mW.

There have been attempts to measure the absolute power in CW mode but they were unsuccessful. There may be several reasons for that, e.g. too noisy environment, faulty optical chopper or lock-in amplifier, wrong experimental setup etc. However, the obtained current-voltage data (not shown) indicated lasing therefore nonworking device could be excluded from possible reasons.

Chapter 5

Thermocompression bonding

The temperature performance is crucial for practical applications of QCL THz. It has been shown that using copper as a waveguide cladding material instead of gold, the former being a better thermal conductor and leading to lower optical losses due to smaller skin depth[3], may improve the temperature performance. As described in section 3.2.2, one of the fabrication steps of a metal-metal waveguide is flip-chip bonding. The devices had been sent to an external company offering thermocompression bonding. Unfortunately, it is costly, time consuming and the company only offers golden bonds. Work has been undertaken to develop an in-house technique to bond QCL chips using gold as well as copper.

5.1 Jig design

The jig parts are drawn in figure 5.1 (top view). A is the bottom plate, on which two chips are placed. B is the thin middle plate with a $10\text{mm} \times 14\text{mm}$ recess used to align the samples on the bottom plate; its thickness ($900\mu\text{m}$) is higher than that of one chip, but lower than two chips, therefore it allows precise alignment along the edges of a rectangular hole in the middle. C and D are two top plates, between which a steel ball bearing (not shown) is placed in a circular recess in order to improve uniformity of the pressure exerted on samples. Parts C and D are almost identical — the only difference is that the bottom side of part C (not visible) has to be polished because it is in contact with the sample.

When the chips are aligned and all the parts are in place, six springs made of stainless steel are used to squeeze the samples between the plates. Six springs are used to ensure uniformity of the pressure on the top element of the jig. The applied force is adjusted to the size of the chips according to Hooke's law. The jig is then placed on a hot plate, heated to 400°C and left for one hour at this temperature. After it cools down, it is disassembled and the samples are annealed for 15 min at 430° .

The quality of the bond is strongly affected by contamination and roughness, therefore special care is taken to maintain cleanness and smoothness of the jig

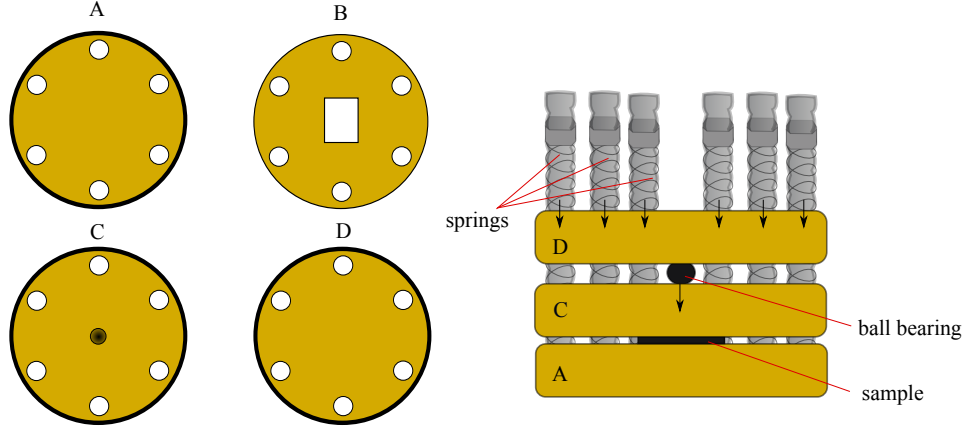


Figure 5.1: **Left:** The jig parts (top view). Part B is used to align the samples and it is only $900\mu\text{m}$ thick. Parts C and D are identical in shape and size. The dark spot in the centre of part C is the recess in which a steel bearing is placed. M6 screws are placed in circular holes near the sides of the parts. **Right:** the jig as seen from the side. Black arrows indicate the force exerted on the jig parts.

and the samples. Anti-seize grease has to be used to prevent screws from being seized at high temperatures — it is essential not to let it contaminate the surface of the plates. Each part of the jig is cleaned in trichloroethylene for an hour and squirted with isopropanol before use. The bonding is carried out in a cleanroom.

5.2 Testing the bond

After the samples are annealed they are stuck with a crystal bond onto another brass plate which is polished regularly in a workshop to ensure $800\mu\text{m}$ thick recess in it. Three steps towards a metal-metal device have been carried out in order to determine the bond quality:

1. Grinding and polishing in a workshop until the sample is $800\mu\text{m}$ thick
2. Etching the sample with citric acid until the etch-stop layer is reached
3. Putting the sample in ultrasonic bath

So far, five bonds in the jig have been done. Table 5.1 summarizes the results of these attempts.

Out of three bonded and tested samples, only one could be used to process QCLs out of it. More data are needed to determine the reproducibility, but clearly some improvements need to be done. In the future, attempts with smaller chips and different pressure will be made.

5. THERMOCOMPRESSION BONDING

number	material	result
1	n ⁺ on n ⁺	Bonded well. No cracks visible.
2	n ⁺ on V-585 MBE material	Bonded well, no cracks. Bond maintained after citric etch and 3 min ultrasonic bath. Processed and obtained 140 um ridge mesas.
3	n ⁺ on V-672 MBE material	Bonded well. No cracks visible. The MBE material came off from its bonded interface during citric etch. Bonded again with the same outcome.
4	n ⁺ on V-585 MBE material	No cracks visible after bonding. MBE material did not stick well after citric etch. Most of the bond came out after ultrasonic bath for 3 min.
5	n ⁺ on V-672 MBE material	Bonded well. Etch and substrate removal pending.

Table 5.1: A summary of the bonds done in the jig. Table courtesy of Yash Shah.

Chapter 6

Conclusions and future work

The work that preceded writing this thesis took around 4 months. Most of this time was spent on cleanroom training and unsupervised fabrication of quantum cascade lasers. Despite looking technical, it is a complex process requiring meticulousness and discipline. Constant exposure to cleanroom procedures and fabrication methods (not only for QCLs) led to gaining valuable skills, difficult to obtain elsewhere because few research groups have their own cleanroom.

For the nearest future, improvement of the solving programs is planned. The software used in this thesis — initially written for BtC QCLs — needs to be adjusted so that it is more transferable to other designs. Also, the calculated frequencies usually do not match exactly those of fabricated lasers, which suggests that processes inside a QCL have not been completely understood yet and need to be investigated thoroughly.

When the solving software is improved, it will allow the group to design and fabricate resonant-phonon QCLs. The Cambridge group has a history of working broadband devices. The RP design is intrinsically broader than BtC, therefore a natural step forward is to investigate this model and try to make a QCL with emission range broader than the recently achieved 380GHz[7].

The performance of THz QCLs has been improving since the first demonstration in 2002. However, it seems that a major breakthrough is needed in order to push the operating temperature near or above 240K (the temperature at which it is possible to electronically cool the device). When it is achieved, THz QCL will be one of the best candidates for a number of THz applications.

Bibliography

- [1] L. AJILI, G. SCALARI, N. HOYLER, M. GIOVANNINI, AND J. FAIST. Ingaas-alinas/inp terahertz quantum cascade laser. *Applied Physics Letters*, **87**:1–3, 2005. [9](#)
- [2] H. E. BEERE, J. C. FOWLER, J. ALTON, E. H. LINFIELD, D. A. RITCHIE, R. KHLER, A. TREDICUCCI, G. SCALARI, L. AJILI, J. FAIST, AND S. BARBIERI. Mbe growth of terahertz quantum cascade lasers. *Journal of Crystal Growth*, **278**:756–764, 2005. [9](#), [14](#)
- [3] M. A. BELKIN, J. A. FAN, S. HORMOZ, F. CAPASSO, S. P. KHANNA, M. LACHAB, A. G. DAVIES, AND E. H. LINFIELD. Terahertz quantum cascade lasers with copper metal-metal waveguides operating up to 178 k. *Optics Express*, **16**:3242–3248, 2008. [26](#)
- [4] F. CAPASSO, K. MOHAMMED, AND A. CHO. Resonant tunneling through double barriers, perpendicular quantum transport phenomena in superlattices, and their device applications. *IEEE J. Quantum. Electron.*, **22**:1853, 1986. [2](#)
- [5] J. FAIST, F. CAPASSO, D. L. SIVCO, C. SIRTORI, A. L. HUTCHINSON, AND A. Y. CHO. Quantum cascade laser. *Science*, **264**:553–556, 1994. [2](#)
- [6] J. R. FREEMAN. *Heterogeneous terahertz quantum cascade lasers*. PhD thesis, University of Cambridge, 2009. [iv](#), [v](#), [4](#), [5](#), [7](#), [8](#), [11](#), [16](#), [20](#), [22](#)
- [7] J. R. FREEMAN, A. BREWER, J. MADO, P. CAVALI, S. S. DHILLON, J. TIGNON, H. E. BEERE, AND D. A. RITCHIE. Broad gain in a bound-to-continuum quantum cascade laser with heterogeneous active region. *Applied Physics Letters*, **99**:241108, 2011. [29](#)
- [8] C. M. HERZINGER, C. C. LU, T. A. DETEMPLE, AND W. C. CHEW. The semiconductor waveguide facet reflectivity problem. *IEEE Journal of Quantum Electronics*, **29**:2273–2281, 1993. [6](#)

- [9] Q. HU, B. S. WILLIAMS, S. KUMAR, H. CALLEBAUT, S. KOHEN, AND J. L. RENO. Resonant-phonon-assisted thz quantum-cascade lasers with metal-metal waveguides. *Semiconductor Science and Technology*, **20**:S228–S236, 2005. [11](#)
- [10] R. F. KAZARINOV AND R. A. SURIS. Possibility of the amplification of electromagnetic waves in a semiconductor with a superlattice. *Sov. Phys. Semicond.*, **5**:707–709, 1971. [2](#), [3](#)
- [11] S. KUMAR, C. W. I. CHAN, Q. HU, AND J. L. RENO. A 1.8-thz quantum cascade laser operating significantly above the temperature of w /kb. *Nature Physics*, **7**:166–171, 2011. [iv](#), [12](#), [13](#)
- [12] L. N. KURBATOV, A. D. BRITOV, S. M. KARAVAEV, S. D. SIVACHENKO, S. N. MAKSIMOVSKII, I. I. OVCHINNIKOV, M. M. RZAEV, AND P. M. STARIK. Far-ir heterojunction lasers tunable to 46.2 microns. *JETP Lett.*, **37**:499–502, 1983. [1](#)
- [13] H. C. LIU. A novel superlattice infrared source. *Journal of Applied Physics*, **63**:2856–2858, 1988. [2](#)
- [14] L. R. RAM-MOHAM. *Finite Element and Boundary Element Applications in Quantum Mechanics*. Oxford, 2002. [11](#)
- [15] C. SIRTORI, F. CAPASSO, J. FAIST, A. L. HUTCHINSON, D. L. SIVCO, AND A. Y. CHO. Resonant tunneling in quantum cascade lasers. *IEEE Journal of Quantum Electronics*, **34**:1722–1729, 1998. [4](#), [5](#)
- [16] M. TONOUCHI. Cutting-edge terahertz technology. *Nature Photonics*, **1**:97–105, 2007. [1](#)
- [17] L. TSU AND R. ESAKI. Superlattice and negative differential conductivity in semiconductor. *IBM Journal of Research and Development*, **14**:61–65, 1970. [2](#), [4](#)
- [18] B. S. WILLIAMS. Terahertz quantum-cascade lasers. *Nature Photonics*, **1**:517–525, 2007. [iv](#), [2](#), [10](#), [11](#)